Color Inserts

This page intentionally left blank

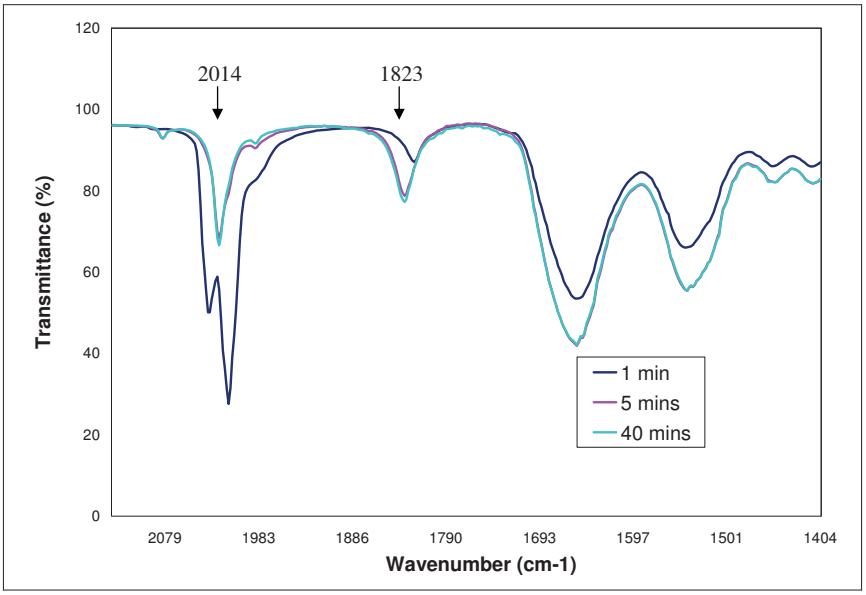

Figure 2.6 FTIR spectrums of iron spider silk sample after different exposure time.

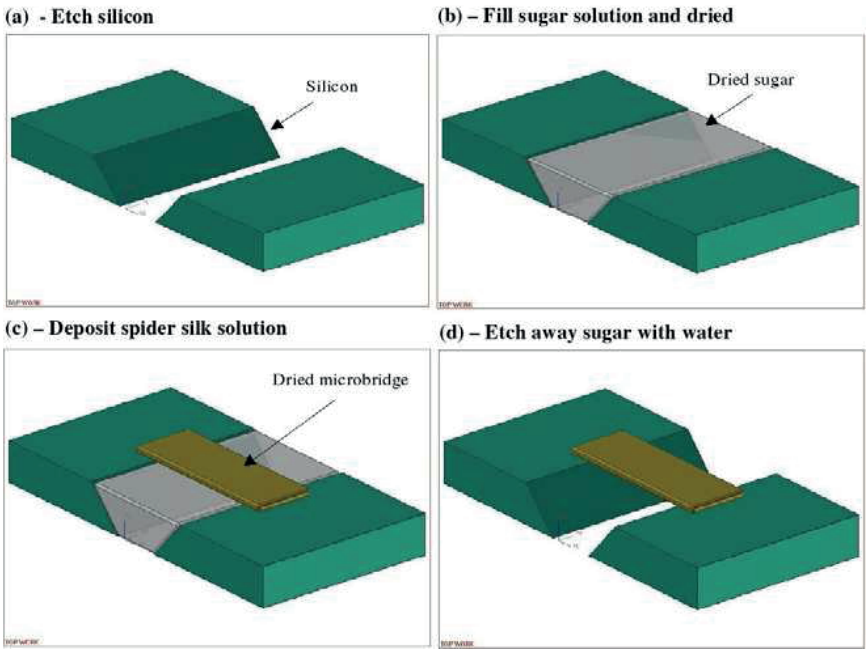

Figure 2.8 Sacrificial etching process steps to fabricate spider silk microbridge.

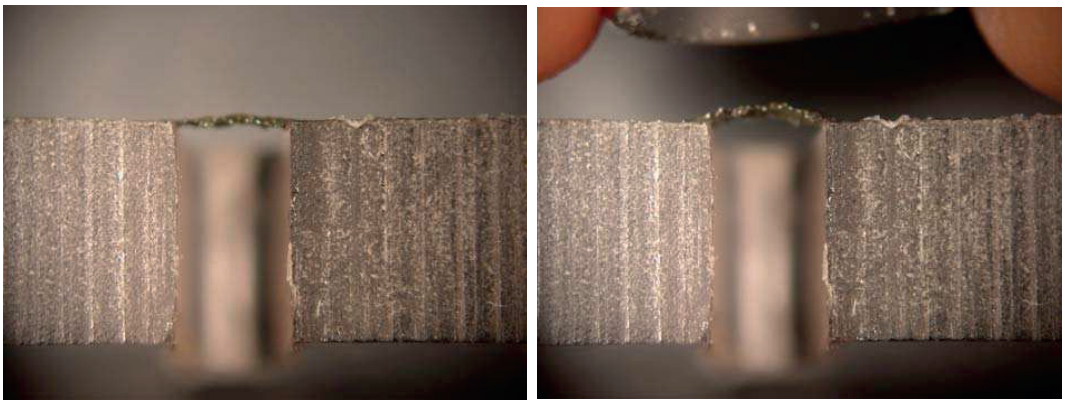

Figure 2.13 Fe/Ni 50%spider silk beam.

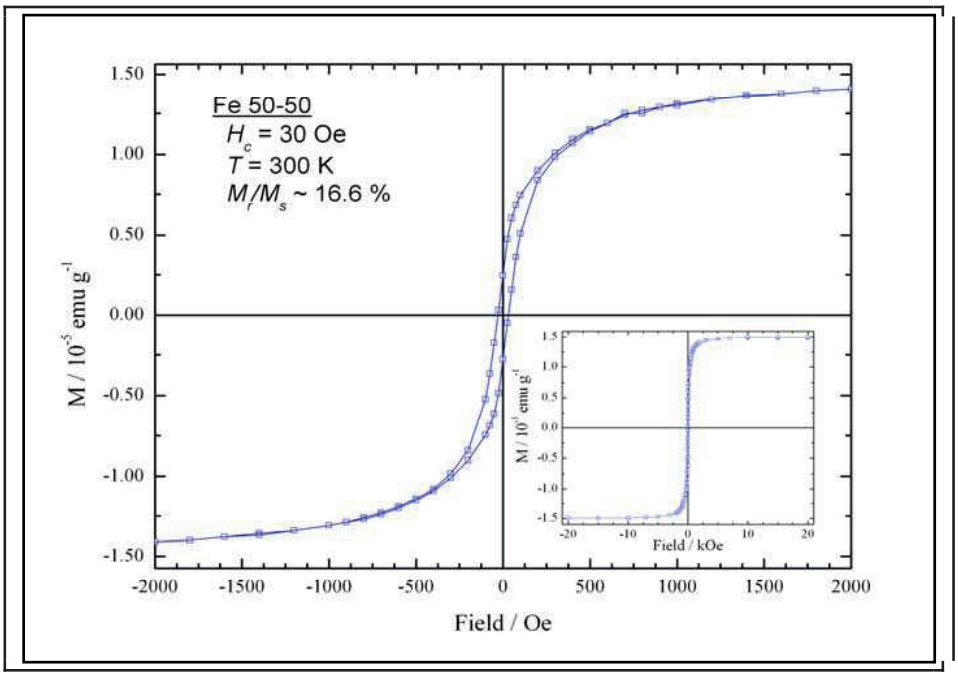

Figure 2.14 Hysteresis curve for 1:1 v/v iron spider silk sample.

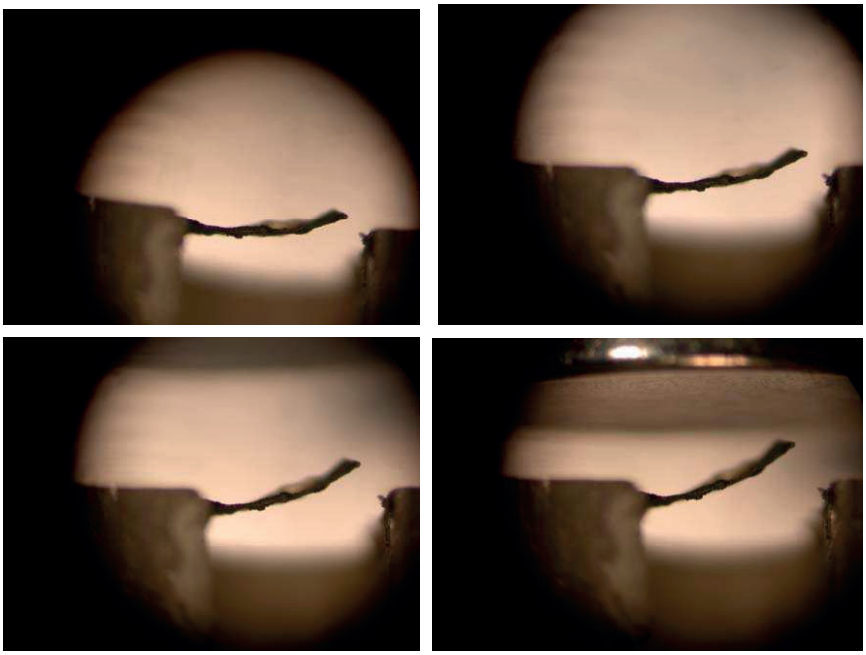

Figure 2.15 Images used to measure bending movement of the beam under increasing magnetic field. Sample size 3.25 × 0.98 × 0.17 mm (*Length* × *Width* × *Thickness*).

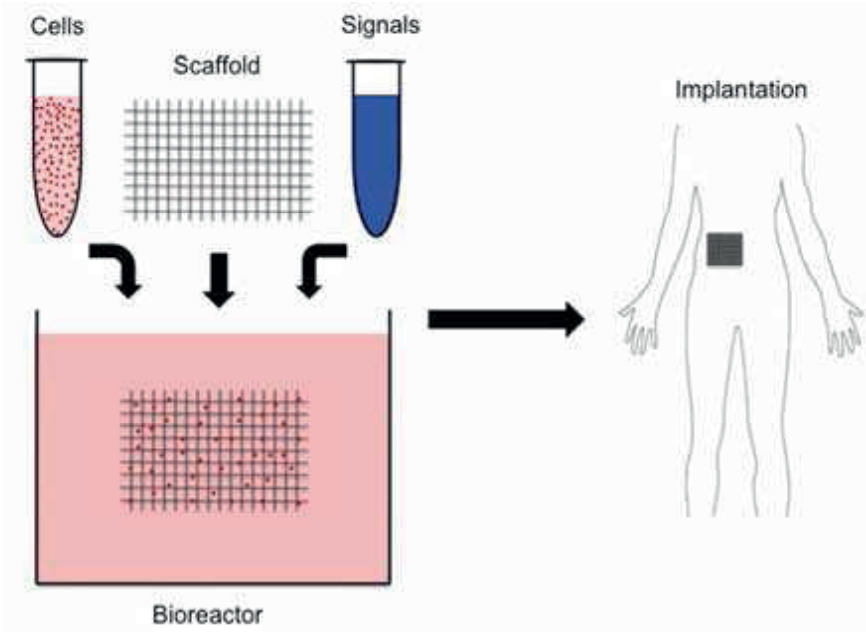

Figure 3.1 The key elements involved in the classic tissue engineering paradigm.

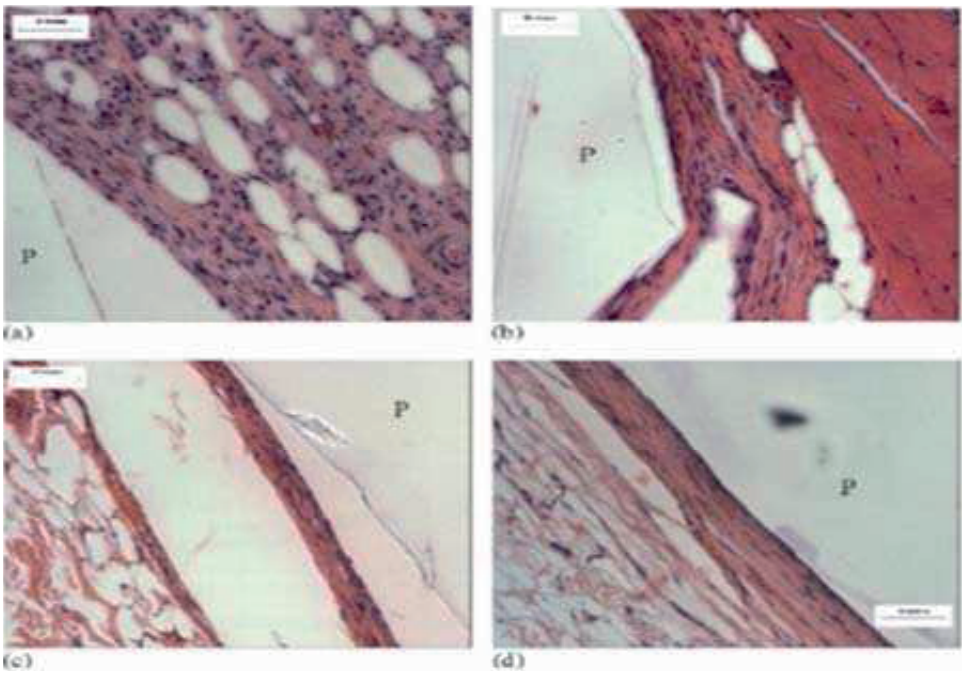

Figure 3.2 Foreign body response of POC (120°C, 2 Pa, 3 d) implanted subcutaneously in female Sprague–Dawley rats (scale bar = 50 μm). Implants and surrounding tissues were harvested after (a) 1 week; (b) 1 month; (c) 2 months; (d) 4 months implantation for H&E staining. "P" represents polymer section. Reprinted from Biomaterials, 27, Jian Yang *et al.*, Synthesis and evaluation of poly(diol citrate) biodegradable elastomers, 1889–1898, 2006, with permission from Elsevier.

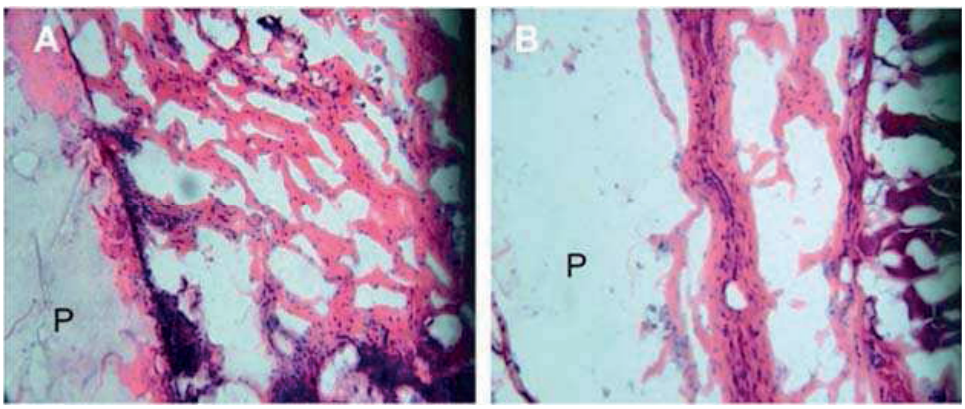

Figure 3.3 Foreign body response of PAMC (POMC 0.8, 20 mins. UV crosslinking) implanted subcutaneously in female Sprague–Dawley rats. Implants and surrounding tissues were harvested after (a) 1 week and (b) 4 weeks. "P" represents polymer section.

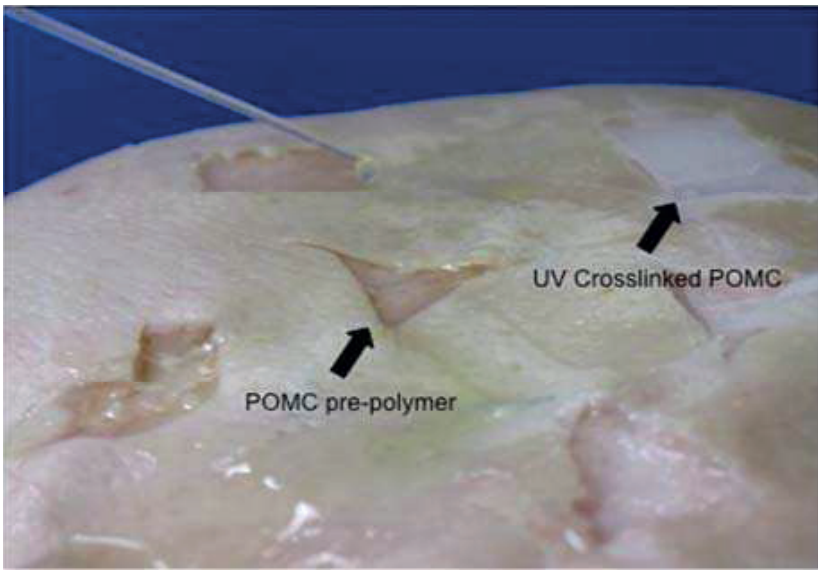

Figure 3.4 Pre-PAMC and ultraviolet crosslinked PAMC on porcine skin.

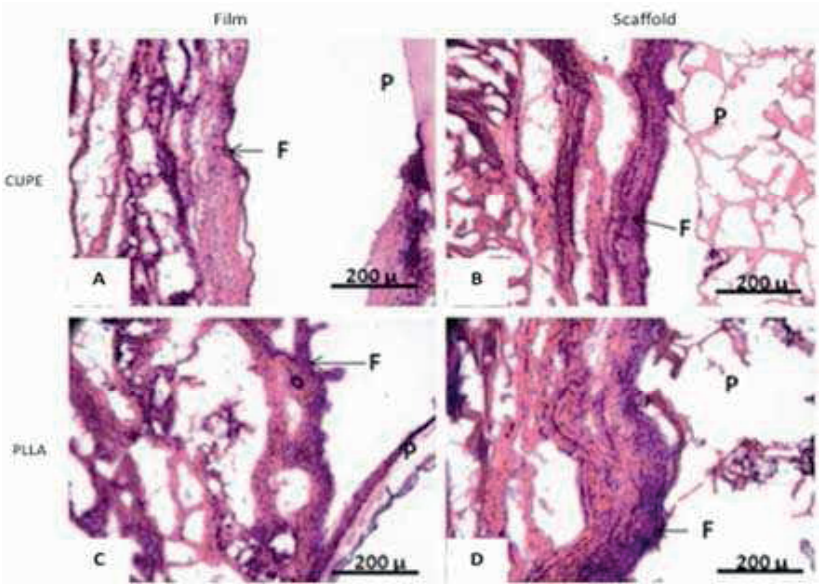

Figure 3.5 Histology of *in vivo* response to CUPE film (A) and scaffold discs (B). PLLA films (C) and scaffolds (D) served as control. P and F are used to indicate the regions of polymer and fibrous capsule respectively. All images were taken at 10x magnification. On the 1 week samples, although all samples were covered by a well defined fibrous capsule, CUPE implants were consistently surrounded by a thinner fibrous capsule as opposed to PLLA implants. In the case of the 4 week implants, overall, all the implants appear to trigger similar extent of tissue responses.

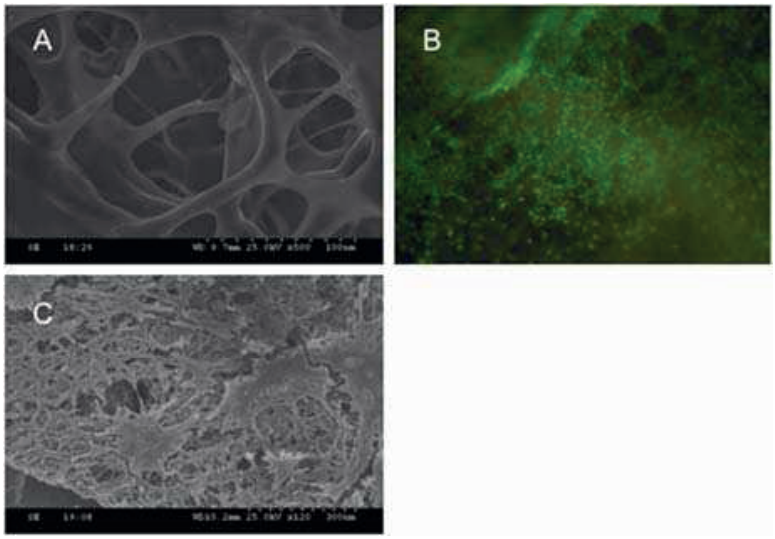

Figure 3.6 SEM images of scaffold surface indicate the presence of well defined pores (A) and even cell distribution of cells on the scaffold (B and C).

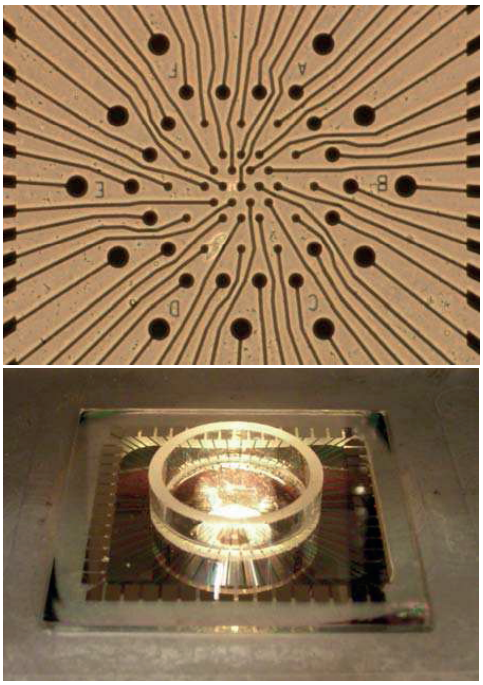

Figure 4.1 One example of a commercially available microelectrode array (Multichannel Systems Hexagonal Array). Neurons or neural tissues are plated on the array surface, top. The circular electrodes can be stimulated and recorded from, but the electrical traces are insulated from neurons plated above. The electrodes are found in the center of the well, which contains culture media to provide cells with nutrients, bottom.

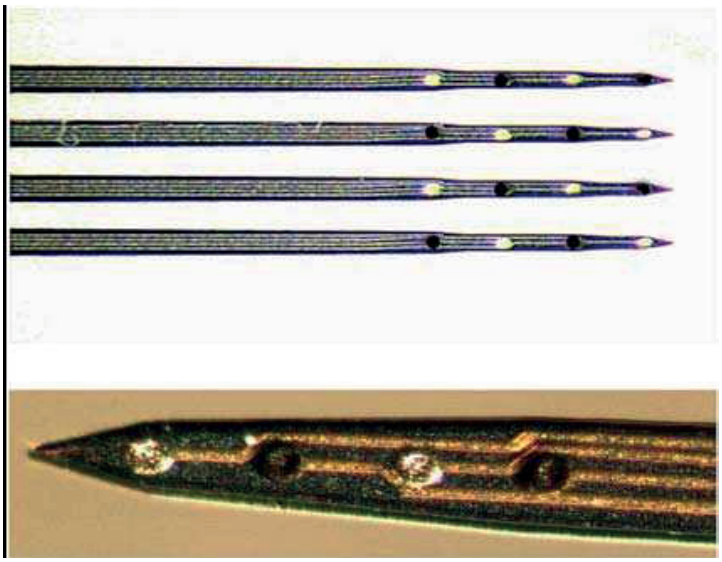

Figure 4.4 The four shanks of a Michigan probe, top; closer image of the four electrodes per shank, bottom. The darker electrode sites in the lower picture have been treated with the conductive polymer poly(3,4-ethylenedioxythiophene) (PEDOT).[32] Reprinted with permission from the *Journal of Neural Engineering*, Ludwig *et al.*, 2006, Vol 3, Issue 1, pp. 59–70.

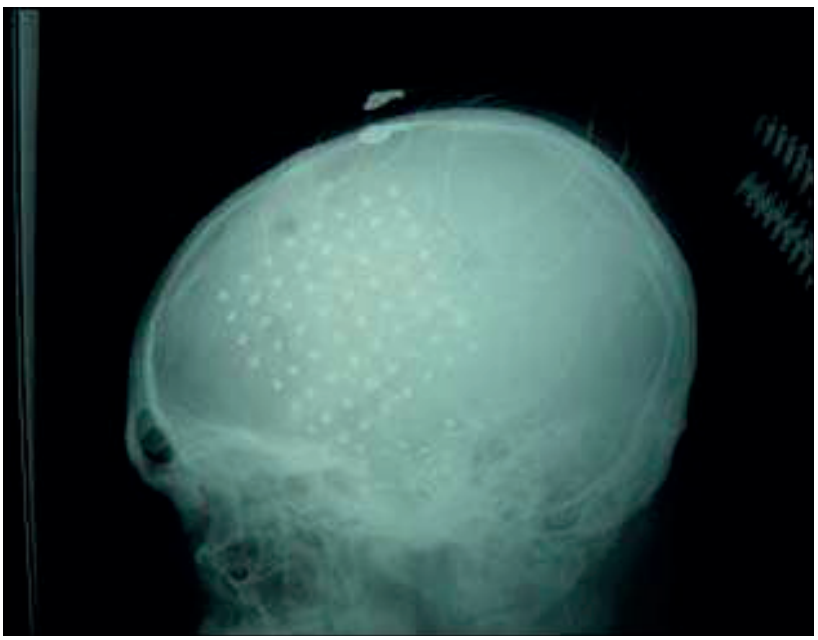

Figure 4.7 An ECoG electrode array located on top of the cortex but inside the skull.[91] Reprinted with permission from the *Journal of Neural Engineering*, Leuthanrdt *et al.*, 2004, Vol 1, Issue 2, pp 63–71.

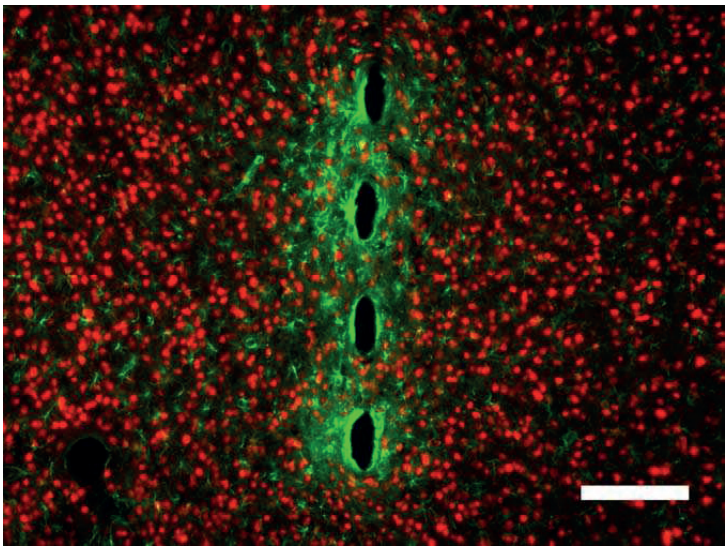

Figure 4.8 The response of rat cortical tissue 8 weeks after insertion. The green stain marks glial fibrillary acidic protein (GFAP), a marker for astrocytes, and the red NeuN stain marks neuron nuclei. The scale bar is 100 micrometers. Notice the astrocytes apparent at the electrode interface, and that the neurons appear further away. Image courtesy of George McConnell, Bellamkonda Lab, Georgia Institute of Technology.

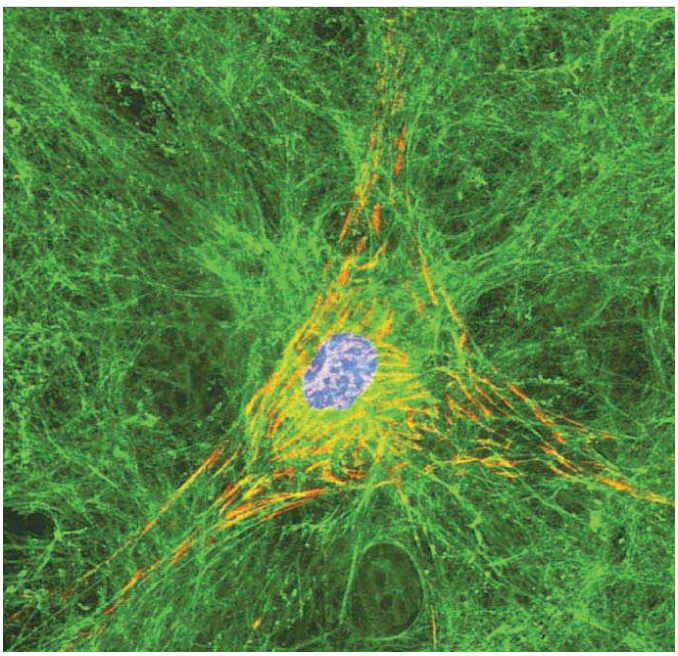

Figure 5.1 A cell in a three-dimensional culture forming links with the scaffold.[2]

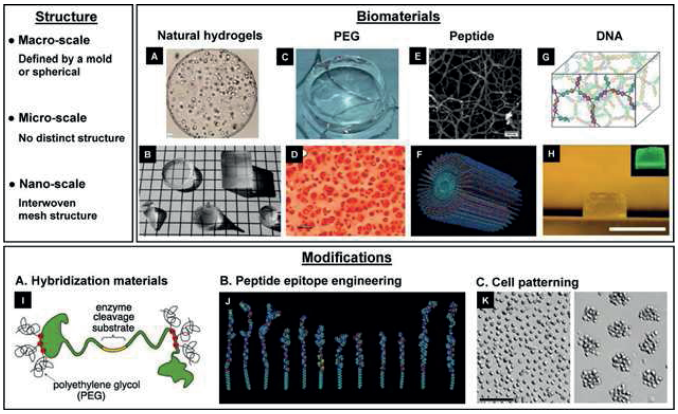

Figure 5.3 Overview of hydrogels used for 3-D cell entrapment.[14]

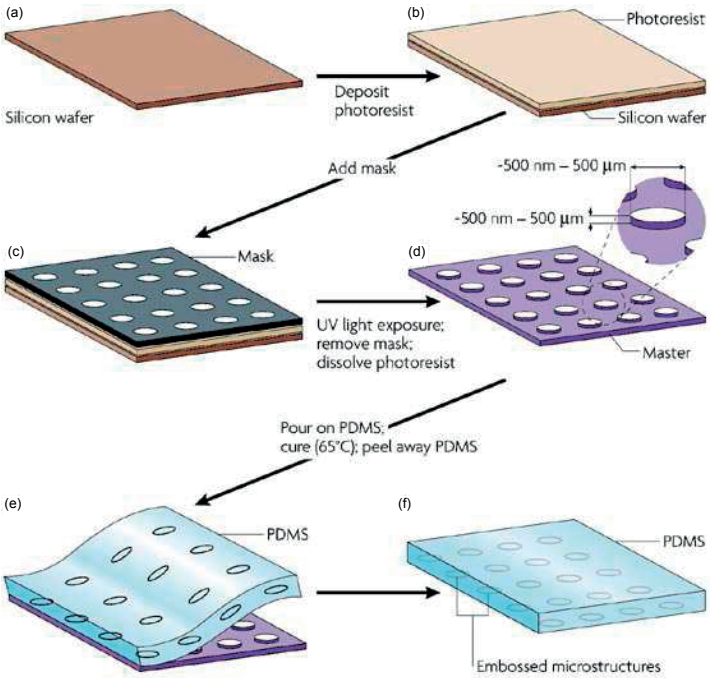

Figure 5.7 Microfabrication of PDMS structures. (a–b) Photoresist is spin-coated on a silicon wafer. (c) A mask is placed in contact with the layer of photoresist. (d) The photoresist is illuminated with ultraviolet (UV) light through the mask. An organic solvent dissolves and removes photoresist that is not crosslinked. The master consists of a silicon wafer with features of photoresist in bas-relief. An expanded view of one of the microfabricated structures with its characteristic critical dimensions is shown. (e) PDMS is poured on the master, cured thermally and peeled away. (f) The resulting layer of PDMS has microstructures embossed in its surface.[47]

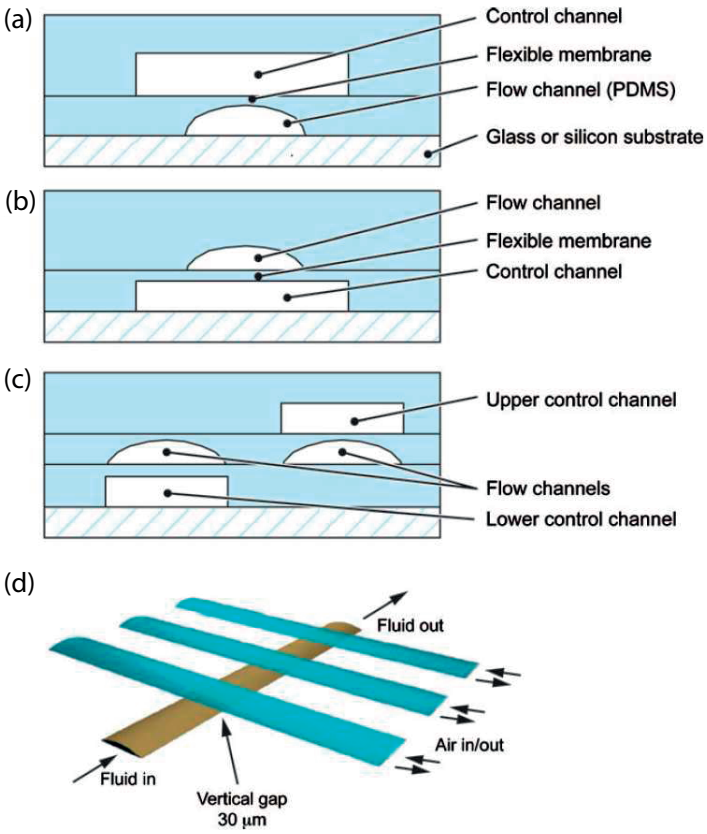

Figure 5.8 For color reference, see page 100.

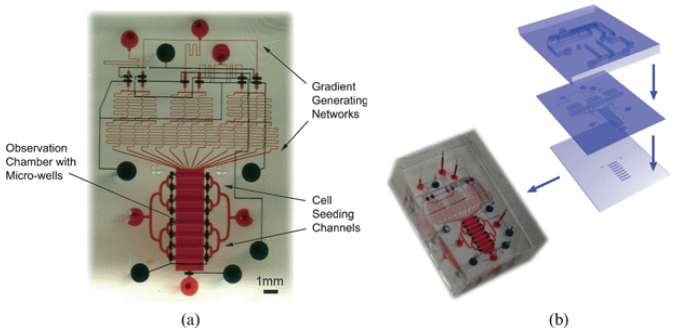

Figure 5.9 (a) A two-layer polydimethylsiloxane (PDMS) push-down microfluidic valve. An elastomeric membrane is formed where the flow channel is positioned orthogonal to the control channel directly above. Fluid flow is out of the page. (b) A two-layer PDMS push-up microfluidic valve where a control channel lies orthogonal to and below the flow channel. (c) A three-layer device with both push-up and push-down valves. (d) Schematic of a linear peristaltic pump using three membrane valves in a series.[53]

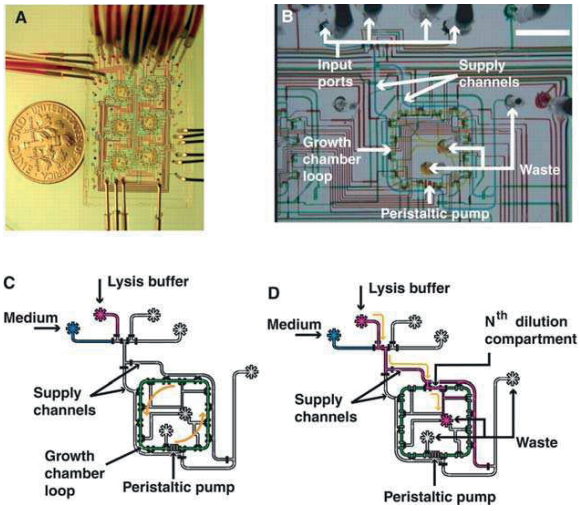

Figure 5.10 (A) Optical micrograph showing six microchemostats that operate in parallel on a single chip. Various inputs have been loaded with food dyes to visualize channels and sub-elements of the microchemostats. The coin is 18 mm in diameter. (B) Optical micrograph showing a single microchemostat and its main components. Scale bar, 2 mm. (C) Schematic diagram of a microchemostat in continuous circulation mode. Elements such as the growth loop with individually addressable connected segments, the peristaltic pump, supply channels, and input/output ports are labeled. (D) Isolation of a segment from the rest of the growth chamber during cleaning and dilution mode. A lysis buffer (indicated in red) is introduced into the chip through the lysis buffer port. Integrated microvalves direct the buffer through the segment, flushing out cells, including those adhering to chamber walls. The segment is then rinsed with fresh sterile medium and reunited with the rest of the growth chamber.[46]

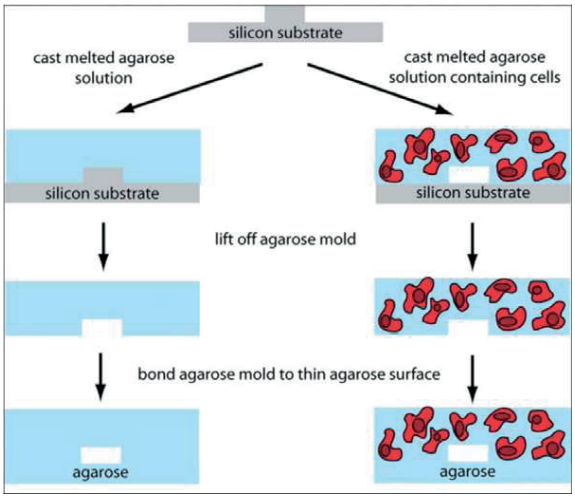

Figure 5.12 Schematic of the fabrication of agarose microfluidic devices with (right) and without (left) embedded cells.[68]

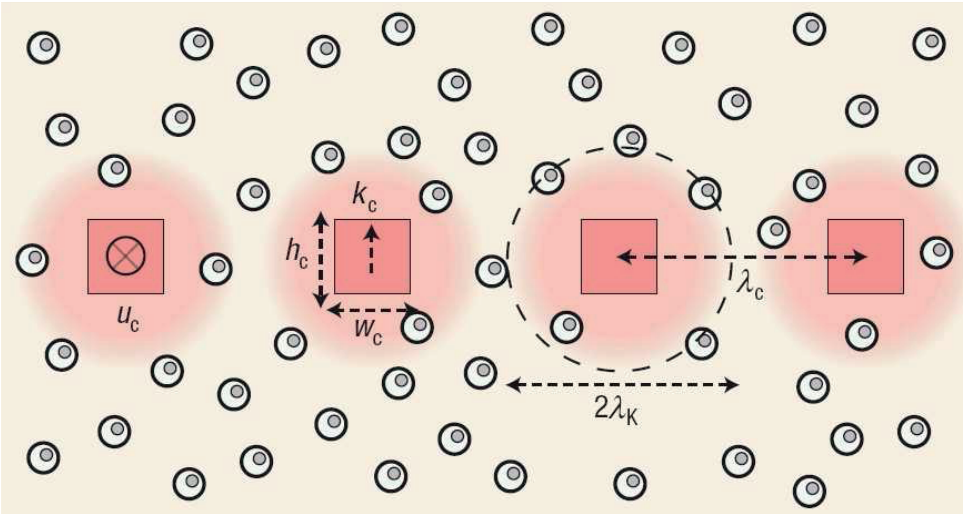

Figure 5.15 Schematic cross-sectional view of a cell-seeded microfluidic scaffold. The dispersed cells (circles) surround the microchannels (squares). The pink shading represents steady-state distributions of solutes. Here, a reactive solute is delivered via the channels and is consumed by the cells as it diffuses into the matrix. λ_K is the Krogh length, λ_c is the interchannel distance, w_c and hc are the microchannel width and height, k_c is the mass transfer coefficient of the flow in the microchannels, and u_c is the speed of the flow in the microchannels.[94]

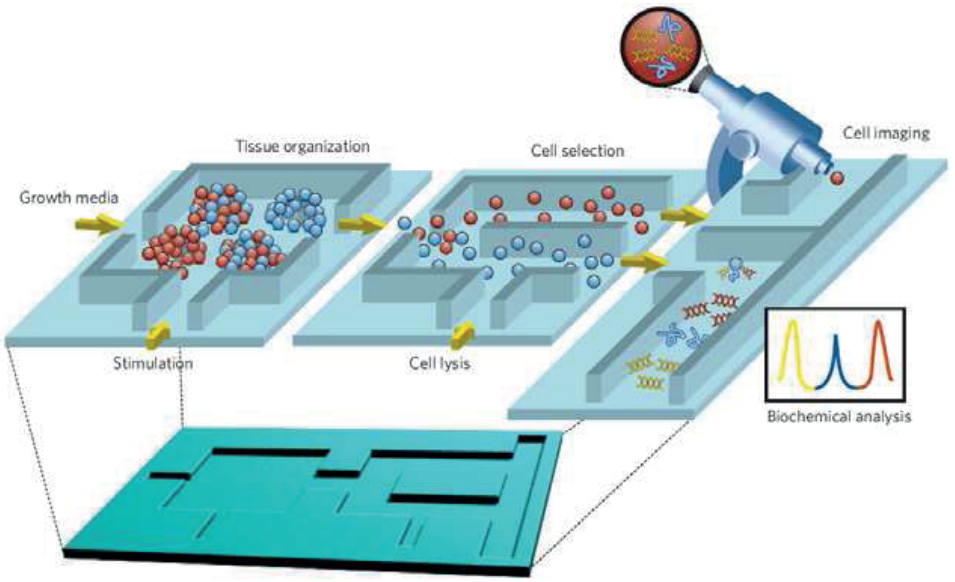

Figure 5.16 Tissue organization, culture and analysis in microsystems. Microsystems can incorporate 3D scaffolds to guide cell growth, microfluidic systems for nutrient transport, different techniques for biochemical analysis (such as image-based analysis), to give multiple functionalities on a single chip.[96]

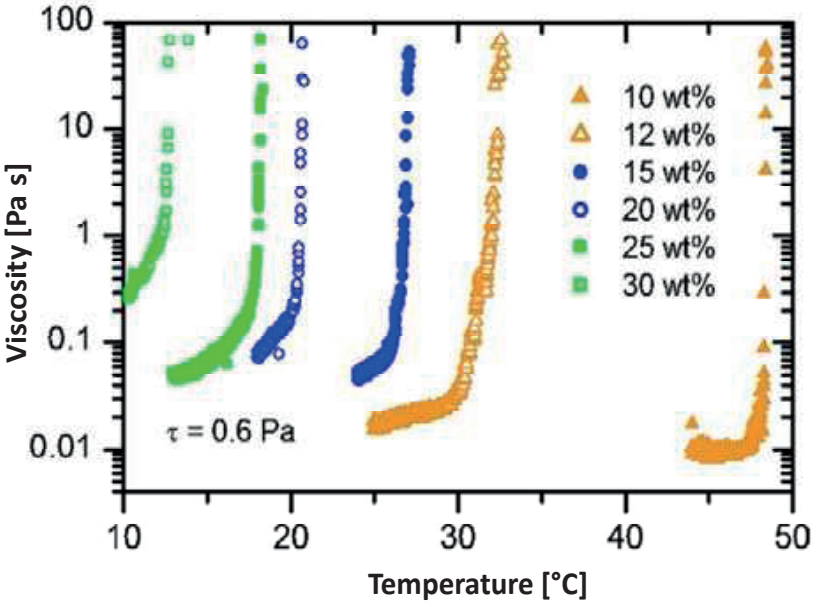

Figure 6.1 Viscosity as a function of temperature for different concentrations of Pluronic F127 in water from cone and plate viscometry at controlled shear stress (0.6 Pa s).[26]

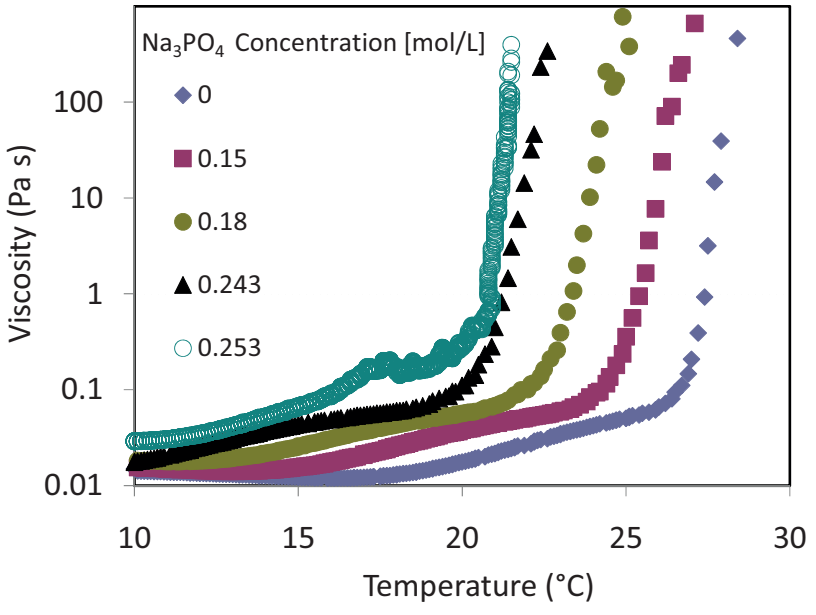

Figure 6.2 Viscosity as a function of temperature for different concentrations of sodium phosphate in a 15 wt% Pluronic F127 solution in water from cone and plate viscometry at controlled shear stress (0.6 Pa s).[110]

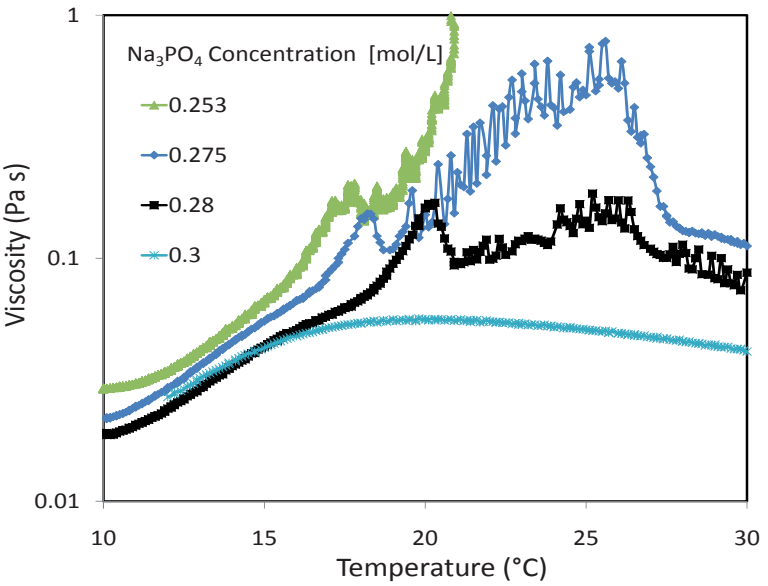

Figure 6.3 Viscosity as a function of temperature for high concentrations of sodium phosphate in a 15 wt% Pluronic F127 solution in water from cone and plate viscometry at controlled shear stress (0.6 Pa s).[110]

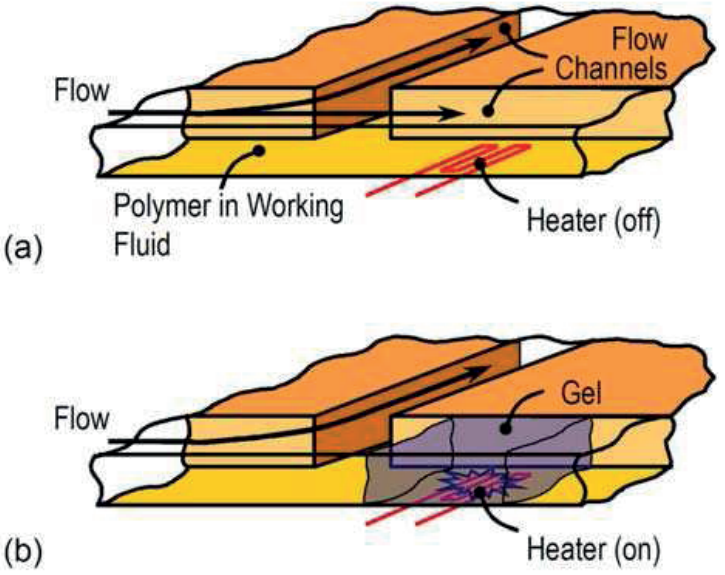

Figure 6.5 A schematic illustration of the principle of an active valve using a thermally responsive fluid in a microfluidic network. (a) Fluid from one channel is diverted into two channels at a channel bifurcation; (b) activating an integrated heater leads to localized gel formation in the corresponding microchannel, which subsequently blocks this channel to flow.

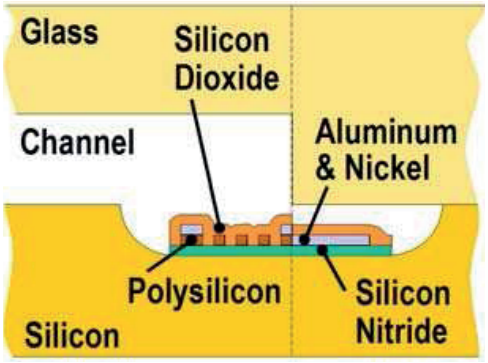

Figure 6.7 A schematic cross-section of the microfluidic device shown in Fig. 6.6. The left-hand side shows the cross-section across a heater in the channel, while the right-hand side shows a cross-section further away from the channel, through an aluminum lead.

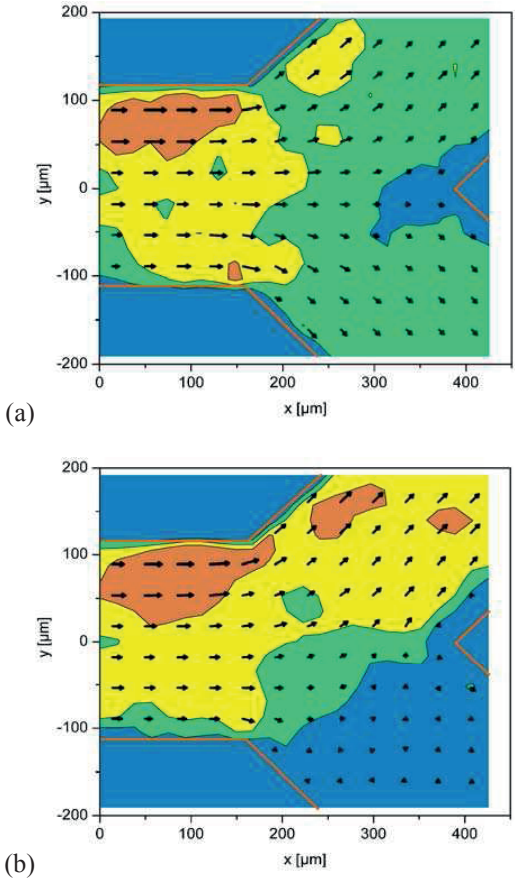

Figure 6.9 The flow field at the channel bifurcation shown in Fig. 6.6. The velocities were evaluated from images of the seed particles as in Fig. 6.8 using PIV; (a) before valve actuation, (b) 33 ms later; blue: below 40 μm/s, green: 40–80 μm/s, yellow: 80–120 μm/s, orange: 120–160 μm/s.

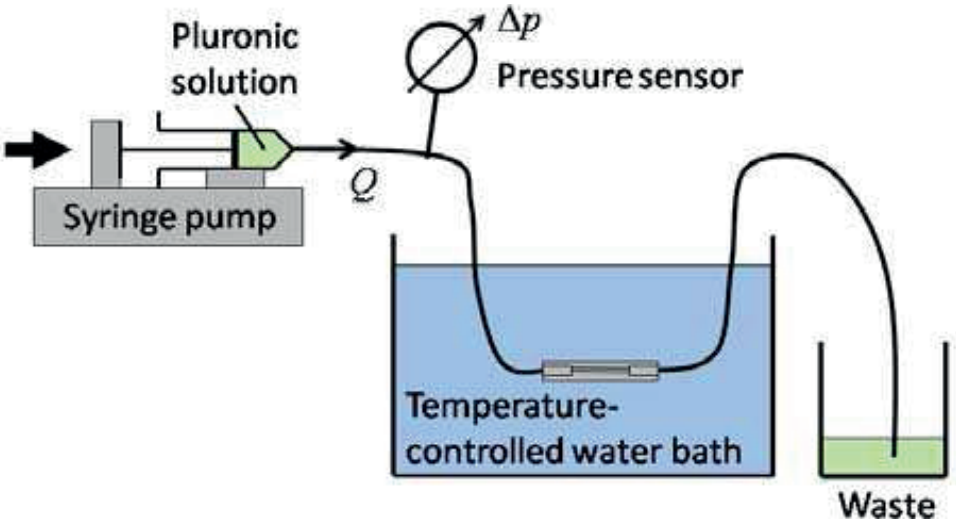

Figure 6.10 Experimental setup for the demonstration of passive flow control using thermally responsive Pluronic solutions at constant flow rate in microchannels.

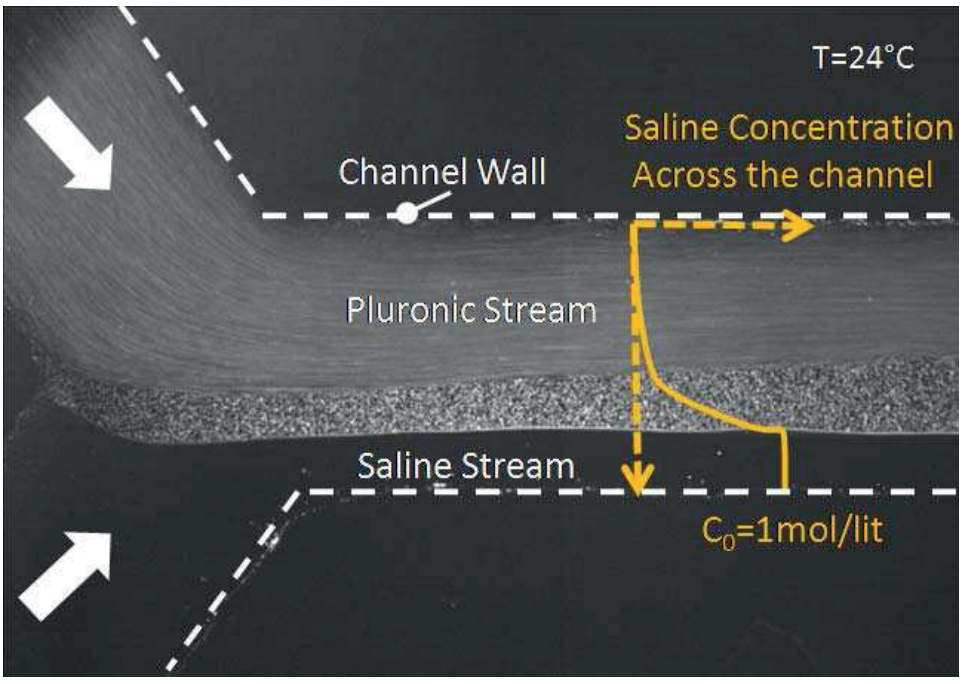

Figure 6.14 Top view of a microfluidic device. Pluronic solution and saline solution are introduced in a 10 μm high microchannel at T_a = 24°C. Gel formation occurs in the center of the channel. The Pluronic stream is seeded with fluorescent particles.

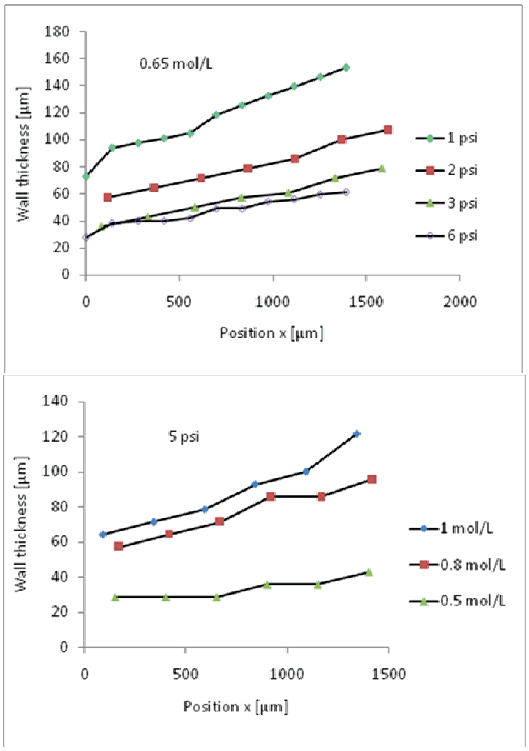

Figure 6.16 Thickness of the gel wall along the channel for different experimental conditions.

Figure 7.5 BioMEMS multi-array prototype implanted subcutaneously in a rodent model. The local environment had encapsulated the device in an attempt to isolate it from the body (28 days post-implantation).

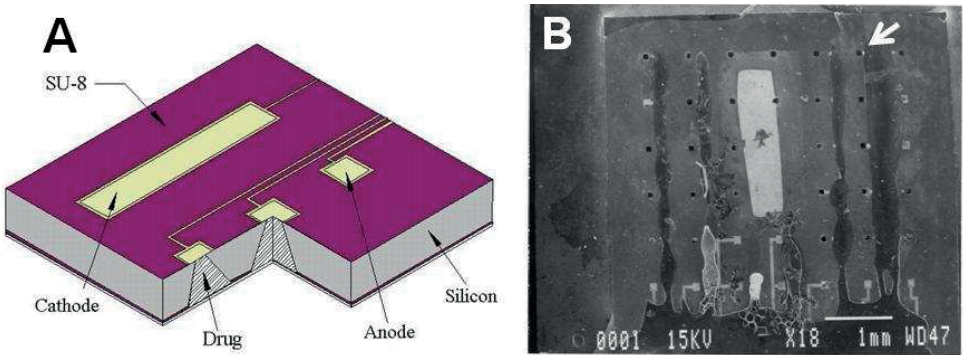

Figure 7.8 BioMEMS micro-array prototype. The inner-reservoir surface area is larger than it appears from a top view (A). The activation of the entire multi-array reservoir system leads to dissolution of the reservoir sealing membrane, release of the drug, and the onset of a "new" inflammatory response initiated by the exposed surface of the inner reservoir (B).

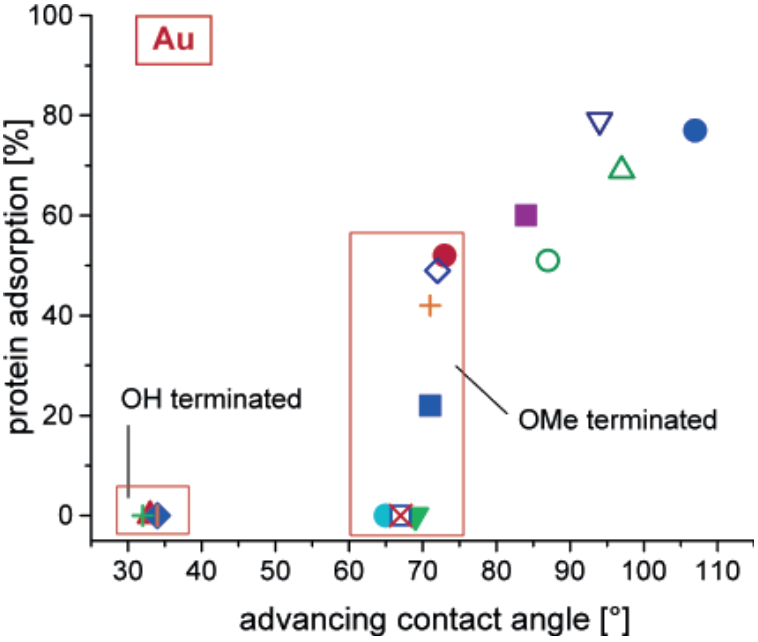

Figure 8.1 Amount of protein adsorption on a given oligoether SAM on gold normalized to the amount of protein adsorbed on a monolayer of hexa-decanethiol on gold (100%) versus advancing aqueous contact angle of the SAM. Symbols: red▲, EG_2OH; orange, EG_3OH; green+, EG_6OH; blue♦, TRI_3OH; blue ■, EG_1OMe; green▼, EG_2OMe; light blue •, EG_3OMe; red ×, EG_6OMe; blue□ , TRI_3OMe; red ×, PRO_2OMe; blue◊, PRO_3OMe; orange +, PRO_4OMe; purpl■, EG_3OEt; green○, EG_6OEt; blue▽, EG_3OPr; green△, EG_6OPr; blue •, EG_3OBu. Images adapted from Ref. 54.

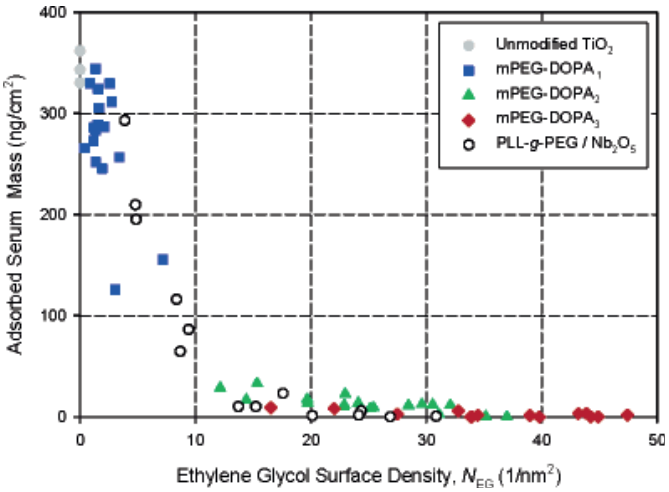

Figure 8.8 Ethylene glycol surface density versus adsorbed serum thickness. Images adapted from Ref. 78.

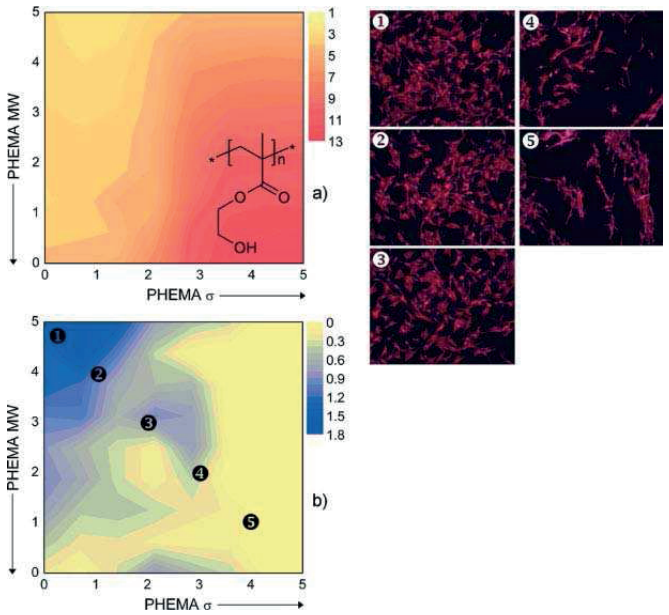

Figure 8.20 Left: contour plots of a) dry thickness of PHEMA in a MW-σ orthogonal PHEMA gradient (scale in nm); b) dry FN thickness in a MW-σ orthogonal PHEMA/FN gradient (scale in nm), the scales depicting the position on the substrate in parts (a) and (b) are in cm. Right: fluorescence microscopy (10x) images of fluorescently labeled MC3T3-E1 cells (nucleus: DAPI blue, cytoskeleton/actin: phalloidin red) cultured on PHEMA/FN gradient substrates. Images were taken at positions on the PHEMA/FN gradient sample marked with the numbers in part (b). The error bars associated with the thickness measurements ($\approx$ 0.1 nm) are smaller than the thickness increments in the contour plots. Images adapted from Ref. 109.

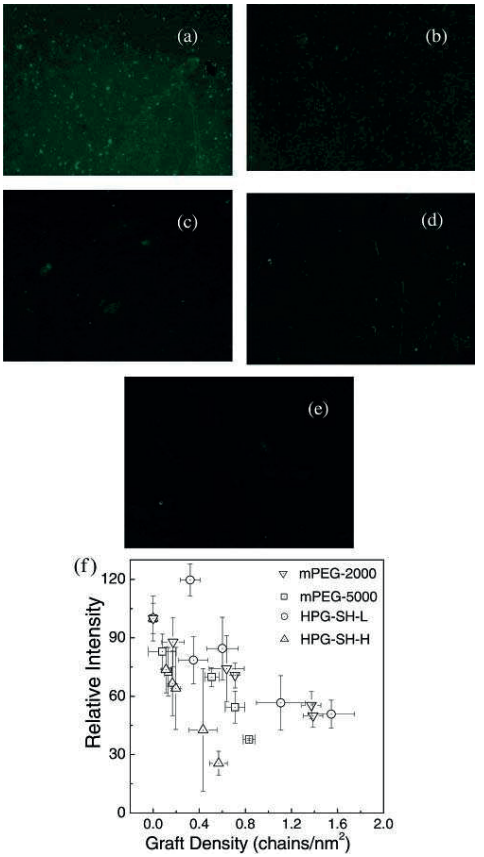

Figure 8.22 Fluorescence photographs of BSA-adsorbed (a) bare gold and (b) linear mPEG-2000-, (c) linear mPEG-5000-, (d) low molecular weight HPG-SH-L-, and (e) high molecular weight HPG-SH-H grafted surfaces. Polymer films were produced by incubating the gold surface in polymer solution at 6 g/L for 16 h. (f) Effect of the graft density on the BSA adsorption of mPEG-, HPG-SH-L-,and HPG-SH-H-grafted surfaces. Images adapted from Ref. 120.

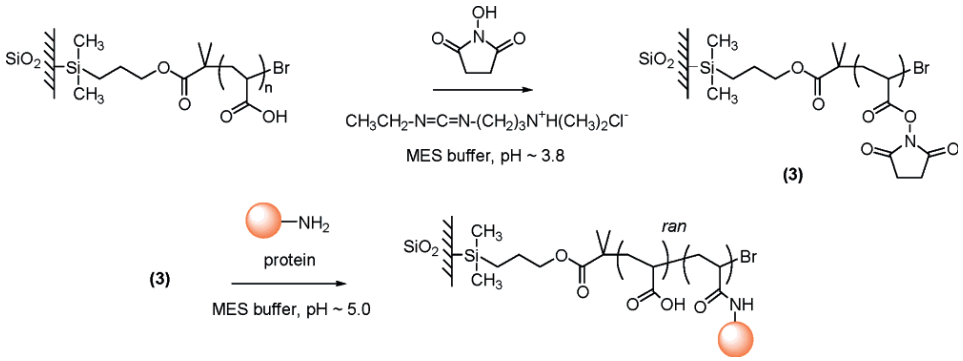

Figure 8.24 Formation of a peptide-modified poly(OEGMA) brush on titanium. Images adapted from Ref. 126.

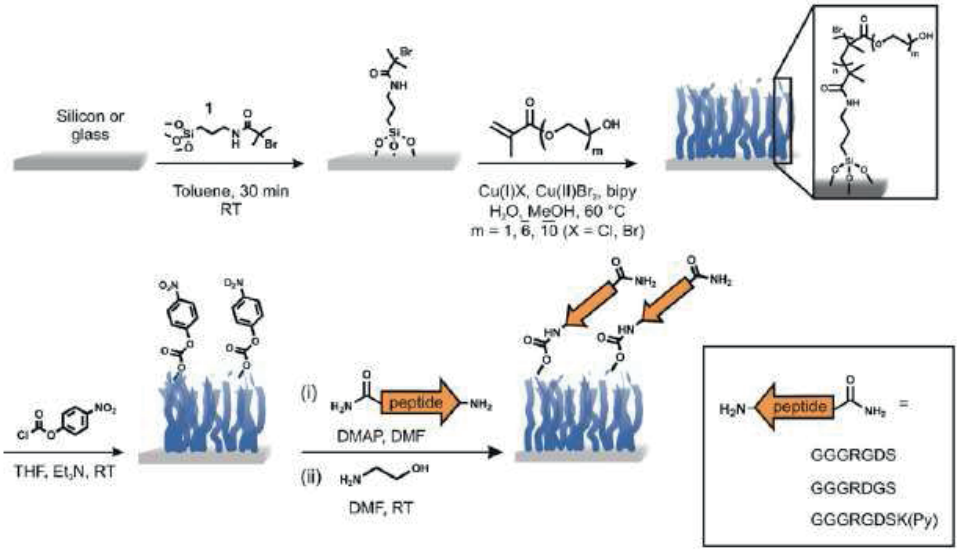

Figure 8.25 RGD functionalized PHEMA and PPEGMA brushes. Images adapted from Ref. 128.

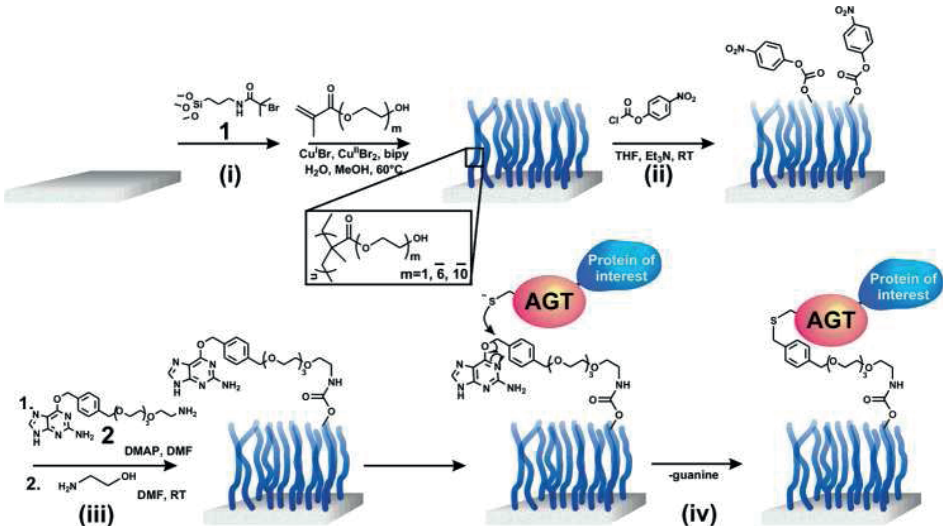

Figure 8.26 Fabrication of protein-functionalized polymer brushes: (i) grafting of ATRP initiator **1** and surface-initiated ATRP; (ii) activation of hydroxyl groups with p-nitrophenyl chloroformate (NPC); (iii) functionalization with benzylguanine derivative **2**and quenching of residual NPC groups; (iv) immobilization of AGT fusion proteins on benzylguanine-displaying surfaces. Images adapted from ref.[129]

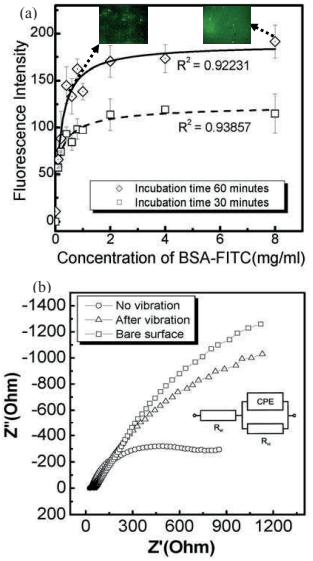

Figure 9.2 (a) BSA adsorption isotherms on a piezoelectric (PZT) surface incubated at 37°C for 1 hour and 30 minutes. The fluorescence intensity was transfer from tri-color to 256 gray scale by Adobe Photoshop 6.0. The intensity is linearly to the quantity of adsorbed BSA, and is a function, which follows the Langmuir isotherm, of BSA concentration. Two inserted photos are fluorescence photos in pointed experimental condition. (b) Nyquist plot of impedance between working electrodes (PZT) and platinum counter electrode. The voltage data (in Z measurement) is corresponding to the reference voltage. The inset is the corresponding equivalent circuit. Reproduced with the permission from Yeh *et al*. (2007).

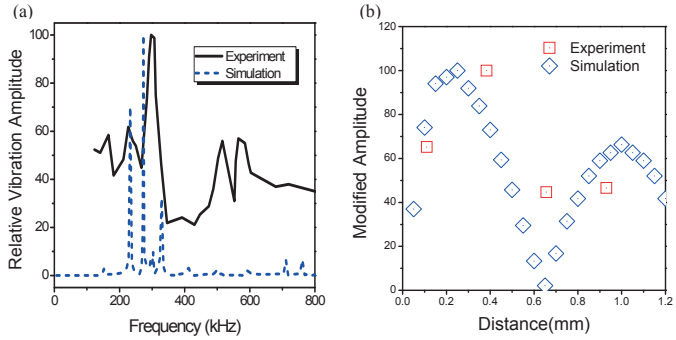

Figure 9.7 (a) The simulation and experimental vibration spectrum of the PZT plate/siliconmembrane. The vibration at 308, 320, 500, and 575 kHz correspond to 1.5, 2.5, 3.5 wavelength bending mode, and longitudinal mode, respectively. (b) The simulation and experimental vibration amplitude distribution across the Si/SiO_2 membrane along the membrane center line. The x axis is given as the distance from the center of the membrane to the left periphery. The half length of the membrane is 1000 μm. Reproduced with the permission from Yeh *et al.* (2008).

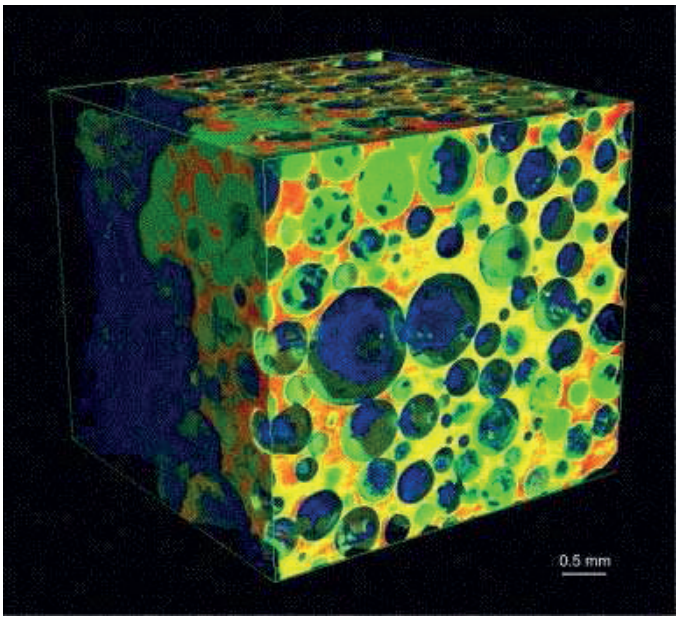

Figure 10.1 3D microCT image of hydroxyapatite scaffold (Engipore) loaded with sheep BMSC and implanted in an immunodeficient mouse, showing newly formed bone (green) onto the inner surface of the scaffold (yellow and red); the organic phase is blue. With permission from.[4]

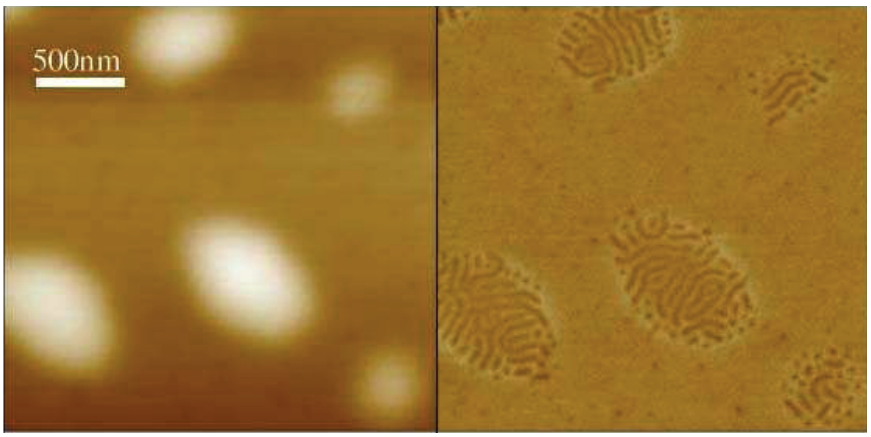

Figure 10.3 Topography and phase image of a poly (styrene-ethylene/butylene-styrene) (SEBS) copolymer treated by solvent annealing. (a) topography image, (b) phase image. The phase image in (b) shows unambiguous resolution of the two different phases of the copolymer. The phase angle contrast of two different copolymers results from the different probe–sample interaction forces. With permission from.[24]

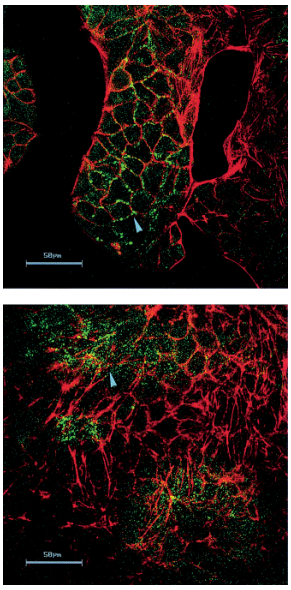

Figure 10.5 Fibronectin formation (green) and actin filament formation (red) in epithelial mHepR1 cells cultured on the biomaterial PHB (below) compared to control cultures (above). Note that in control cultures the actin filaments are structured in fibrils showing colocalization with fibronectin (arrow head) in contrast to PHB cultured cells, where the organization of actin filaments is more irregular and the colocalization of fibronectin with actin is lost (arrow head) (CLSM images taken with LSM 410, Carl Zeiss Jena). With permission from.[33]

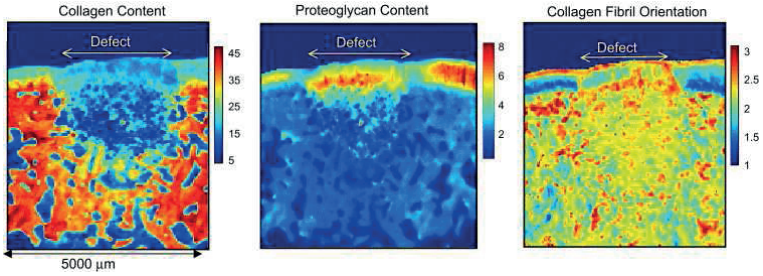

Figure 10.9 FT-IR images of rabbit osteochondral defect at 6 weeks post-repair with TP 508 protein. The defect repair cartilage has lower collagen content (amide I area) compared to the adjacent articular cartilage, but also has regions with PG content (PG sugar ring C-O absorbance (985–1140 cm^{-1}) of a similar magnitude to that in the native cartilage. There is some orientation present in the repair cartilage, as evidenced by the layer of fibrils parallel to the surface. For the orientation data, the boundaries on the color bar indicate the three collagen fibril orientation categories with respect to the articular surface, corresponding to amide I/amide II peak area ratios >2.7 (parallel fibrils), between 2.7 and 1.7 (random fibrils), and <1.7 (perpendicular fibrils), respectively. With permission from.[53]

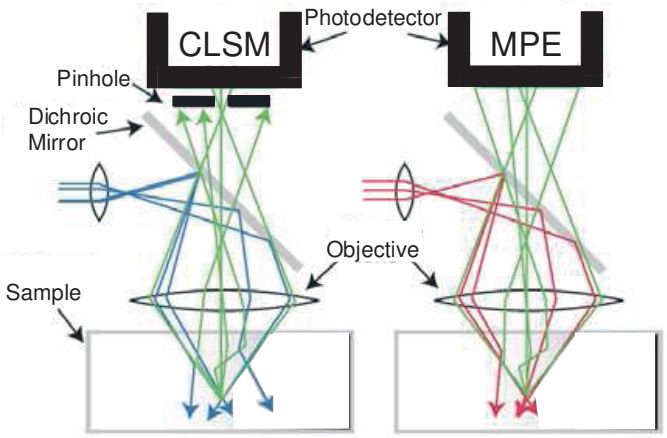

Figure 10.10 Comparison of a conventional confocal microscope (CLSM) with a multi-photon excitation (MPE) microscope.

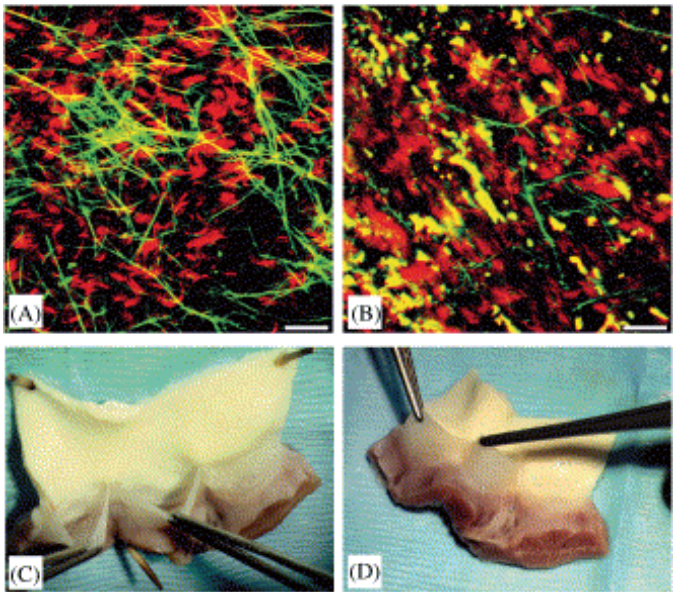

Figure 10.11 Overlay of optical sections showing elastic fibers (green) and collagen (red) of two TE valve leaflets, cultured under different conditions within the bioreactor system. The differences between the tissue states were only explicitly verifiable by the use of the MPE images. (A) TE heart valve, exposed to defined physical signals with a fixed frequency (1 Hz) and pressure conditions (3 l/min and 60/40 mm Hg), show normal extracellular matrix structures (bar: 20 µm). (C) Corresponding macroscopic appearance of the TE valves. (B) TE leaflet, exposed to supra-physiologic (>200 mm Hg) pressures, revealing an impaired matrix formation and a high amount of cell detritus (yellow). (D) Corresponding macroscopic pictures. With permission from.[72]

This page intentionally left blank

Index